

Available online at www.sciencedirect.com

# ScienceDirect

Procedia CIRP 00 (2019) 000-000



18th CIRP Conference on Modeling of Machining Operations

Investigation on the scale effects of initial bulk and machining induced residual stresses of thin walled milled monolithic aluminum workpieces on part distortions: experiments and finite element prediction model

D. Weber<sup>a\*</sup>, B. Kirsch<sup>a</sup>, C.R. Chighizola<sup>b</sup>, J.E. Jonsson<sup>b</sup>, C.R. D'Elia<sup>b</sup>, B.S. Linke<sup>b</sup>, M.R. Hill<sup>b</sup>, J.C. Aurich<sup>a</sup>

<sup>a</sup>Institute for Manufacturing Technology and Production Systems, TU Kaiserslautern, Gottlieb-Daimler-Str., 67663 Kaiserslautern, Germany <sup>b</sup>Department of Mechanical and Aerospace Engineering, University of California, One Shields Avenue, Davis, CA 95616, USA

#### Abstract

Thin walled monolithic milled aluminum workpieces are commonly used in the aerospace industry, because of their good properties such as a high overall strength-to-weight ratio. After machining those parts distortions occur. Residual stresses (RS) are the main driver for those distortions. Two types of RS, the initial bulk residual stresses (IBRS) and the machining induced residual stresses (MIRS), contribute to the part distortion. In this study, the scale effects of each RS type and their combined effects on the distortion of milled thin walled aluminum workpieces are evaluated for different wall thicknesses, different IBRS conditions and different MIRS. In this context a finite element model (FEM) is developed to predict the distortion due to the measured RS. A 3D linear elastic model, considering both types of RS as input is presented. The simulation outcome is validated by experiments.

It was found that both RS types contribute to part distortion. For parts containing high IBRS, those IBRS dominate the distortion. For stress relieved parts, containing low IBRS, the MIRS dominate the distortion. The investigations showed that the shear RS induced by machining are crucial for the distortion. The developed FEM model is able to predict the distortion due to both RS types.

© 2021 The Authors. Published by ELSEVIER B.V.

This is an open access article under the CC BY-NC-ND license (https://creativecommons.org/licenses/by-nc-nd/4.0) Peer-review under responsibility of the scientific committee of the 18th CIRP Conference on Modeling of Machining Operation *Keywords*: Type your keywords here, separated by semicolons;

# 1. Introduction

The aerospace industry demands for improved part designs in order to make aircrafts lighter, stronger and more fuel efficient [1]. Hereby, a maximum rigidity of components at minimum material thickness is desired. Machining of monolithic thin walled components is one way to achieve the advantages of high-performance designs, such as a high overall strength-to-weight ratio and an improved fatigue life [2]. Hereby up to 90 % of the initial material is removed [3]. Although the machining of monolithic components results in low weight structures to maximize energy and efficiency, distortions of the final part can occur. High costs due to the necessary quality control,

remanufacturing or even part rejection are the results [4]. Residual stresses (RS) are the main driver for the distortion of those parts, which are typically distinguished into two types [5]. First, there are the initial bulk residual stresses (IBRS), which exist in the blank material because of upstream processes like casting, rolling, and heat treatments (e.g. quenching). The second type are the machining induced residual stresses (MIRS), which are introduced into the material during the machining process [5].

Research was done focusing on the part distortion from RS. From the experimental perspective there is an agreement in the literature that IBRS are responsible for the distortion of thick

<sup>\*</sup> Corresponding author. Tel.: +49-631-205-5911. E-mail address: daniel.weber@mv.uni-kl.de

aluminum workpieces [5]. However, when it comes to the distortion of thin walled aluminum workpieces, different results are found. Huang et al. [6] found that for milling 3 mm thin walled AA7050-T7451 structures the IBRS are responsible for 90 % of the distortion, while MIRS account for the remaining 10 %. Yang et. al. [3] came to the same conclusion, that IBRS are dominating, while investigating the milling of AA7075 structures. But here it has to be considered that magnitudes of IBRS were significantly higher, because material which has not undergone any stress relief process was used. In contrast, Huang et al. [7] concluded, that for milling 2 mm thin plates out of AA7050-T7451 blocks, MIRS were the primary cause for the distortion. Furthermore, different critical values have been set for material thicknesses (3 or 4 mm) in the literature to determine when MIRS play the leading role [5].

Finite element method (FEM) simulations are often used to predict the part distortion due to IBRS and/ or MIRS of milled thin walled monolithic aluminum workpieces. Typically, those simulations are characterized by linear elastic FEM models, where the RS are known and used as an input to predict the part distortion [1,2,6,8,9,10,11]. The models differ in that some considered the material removal process [6,10,11] by element deletion and others [1,2,8,9] applied the RS directly to the finished part shape. The re-equilibrium of the RS causes the workpiece to distort. The RS required for the simulation were obtained by measured data, analytical models or numerically [10]. All these investigations, whether numerically or experimental, showed that the parameters

- magnitude of IBRS (stress relieved or not)
- wall thickness
- magnitude and penetration depth of MIRS

are crucial for making any statements on what RS type contributes more to part distortion of aluminum alloys. But yet their mutual impact on part distortion was not analyzed in detail. Therefore, this study evaluates the effect of each RS type and their combined effect on the distortion of milled thin walled aluminum workpieces by considering different IBRS conditions, different machining conditions and different wall thicknesses. Moreover, a finite element model based on the above described approach is developed to predict the distortion due to the RS and to extend the knowledge gained from experimental investigations. A 3D linear elastic model, considering both types of RS as input, is presented. The simulation outcome is validated by experiments.

#### 2. Methods

# 2.1. Experiment

A structure of the dimension 200x98x20 mm³ with one rib in the middle, surrounded by two pockets, which resembles a down scaled thin walled rib type component typically used in the aerospace industry, is milled out of a 206x102x28.5 mm³ aluminum block (see Fig.1). Two different IBRS conditions (quenched AA7050-T74 parts with high IBRS H and stress relieved AA7050-T7451 parts with low IBRS L) [12], two different machining conditions (M1 with lower MIRS, and M3 with higher MIRS – M2 is another machining mode, not included in present paper but in [14]) and two different wall

thicknesses ( $T_1$ =7 mm and  $T_2$ =3 mm) are investigated in order to demonstrate the scale effects of both types of RS and their combined effect on the part distortion (see Table 1). The following configurations are investigated:

- effect of IBRS (high IBRS H, T<sub>2</sub>= 7 mm, Mode 1: H7M1)
- effect of MIRS (L3M1 and L3M3)
- effect of both RS (H3M1 and H3M3)

Each configuration was machined three times for examining the reproducibility (A, B, C), which resulted in 15 experiments in total. Parts with the same IBRS configuration came from the same batch.

Table 1. Overview of machined samples

	Low IBRS (L) AA7050-T7451	High IBRS (H) AA7050-T74
T <sub>1</sub> 7 mm, Mode 1		H7M1-A, -B, -C
T <sub>2</sub> 3 mm, Mode 1	L3M1-A, -B, -C	H3M1-A, -B, -C
T <sub>2</sub> 3 mm, Mode 3	L3M3-A, -B, -C	H3M3-A, -B, -C

For the 3 mm (7 mm) wall thickness about 84 % (67 %) of the initial material was removed. The following manufacturing steps were conducted on a 5-axis DMG Mori DMU 70 CNC<sup>1</sup> machine with different clamping devices to machine those components (see Fig. 1):

- step 1: Side milling in side clamps
- step 2: Face milling of backside in side clamps
- step 3: Face milling of top in vise
- step 4: Drilling holes in vise
- step 5: Milling of pockets (M1/M3) in side clamps, screws

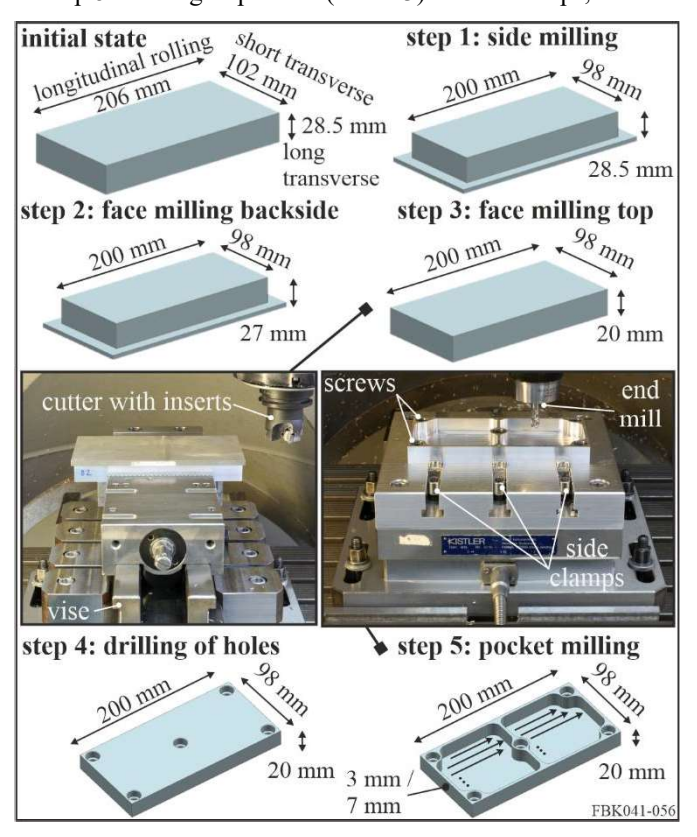


Fig. 1. Manufacturing steps and experimental set up [modified from 15]

Two different tools, a cutter with indexable inserts to face mill the top and backside surface (step 2, 3) and a regular end mill to side mill the walls (step 1) and mill the pockets (step 5), were used. The material properties of the tools can be found in Table 2. Dry down milling was carried out for all milling steps. An external cooling strategy was used for drilling in step 4 (d = 9 mm, n = 2000 rpm,  $v_f$  = 500 mm/min).

Table 2. Tool properties

	Kennametal <sup>1</sup>	Sandvik <sup>1</sup> R590-	
	F3AA1200AWL	050HA6-11M	
type	end mill	index. inserts R590-	
		110504H-NL H10	
diameter	12 mm	50 mm	
material (max. grain	10 % Co, 0.6 % Cr,	cemented carbide (not	
size)	89,4 % WC, (3 μm)	specified)	
flutes/ inserts	3	2	
coating	-	-	
cutting edge radius	-	0.4 mm	
(functional) length	76 mm	71 mm	
helix angle	45°	-	

The machining parameters are listed in Table 3. The milling of the different layers of the pockets was done in alternating order in zig strategy (paths from left to right, see Fig. 1). Side clamps and screws were chosen for clamping while milling the pockets to prevent the bottom surface from distortion before the workpiece was completely finished. Before (Pre-) and after step 5 (Post-) the backside surface was measured with the coordinate measuring machine Tesa micro Hite 3D DCC<sup>1</sup> with a repeatability limit (ISO MPE-p) of 3.5 μm to determine the distortion caused by the RS. A spacing of the measured points of 2 mm with a distance to the edge of 1 mm was chosen, which resulted in 4900 measurement points in total. The final part distortion was analyzed by first leveling (fitting polynomial plane of order 1x1 and subtracting it) each data set and then subtracting the Pre- from the Post-data, similar to the approach presented in [18]. Finally, the resulting surface was set to zero height at its minimum (average of lowest 10 measured points).

Table 3. Machining parameters

	step 1	step 2 and 3	step 5
tool	end mill	index. inserts	end mill
cutting speed $v_{\rm c}$	450 m/min	730 m/min	200 m/min
feed per tooth fz	0.055 mm	0.2 mm	0.04 mm (M1) 0.2 mm (M3)
depth of cut a <sub>p</sub>	5x 4.4 mm	1.5 mm (back)	4x 2.5 mm (T1)
		5x 1.4 mm (top)	5x 2,8 mm (T2)
finishing ap	22 mm		3 mm (T1, T2)
width of cut ae	2.5 mm	$2 \times 40 \text{ mm}$ and	4 mm
finishing a <sub>e</sub>	0.5 mm	18 mm (back), 3 x 34 mm (top)	

It is assumed that the main contribution of the MIRS to part distortion is caused by milling the pockets. Here, two different milling parameter sets, one "aggressive", introducing more compressive MIRS with deeper penetration depth (M3), which is a typical MIRS depth profile found in the literature for milling aluminum alloys [5], and one introducing less MIRS with

shallower penetration depth (M1 – lower feed), were chosen (see Fig. 2). The MIRS resulting from those machining sets were measured via incremental hole-drilling (HD) method [13]. The MIRS profiles of both modes are shown in Fig. 2 and represent the average of 9 HD measurements per machining mode, measured on different samples (for more details see [14,15]). Furthermore, the MIRS on the backside and the top of the sample, resulting from face milling, were measured as well (average of 4 HD measurements) (see Fig. 3).

The IBRS of the low and high stress configuration were measured via the slitting method [16, 17] using wire electric discharge machining. The results are displayed in Fig. 4.

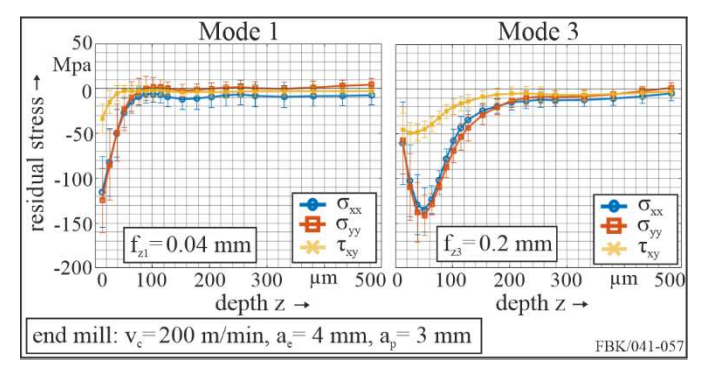


Fig. 2. MIRS depth profiles for machining M1 and M3, where x-corresponds to the feed direction and y- to the orthogonal feed direction

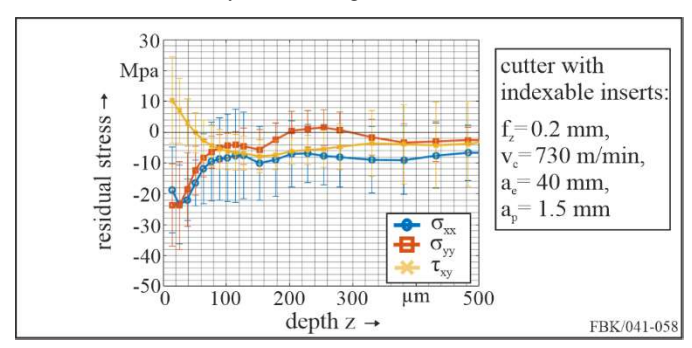


Fig. 3. MIRS depth profiles for machining backside with index. inserts, where x-corresponds to the feed direction and y- to the orthogonal feed direction

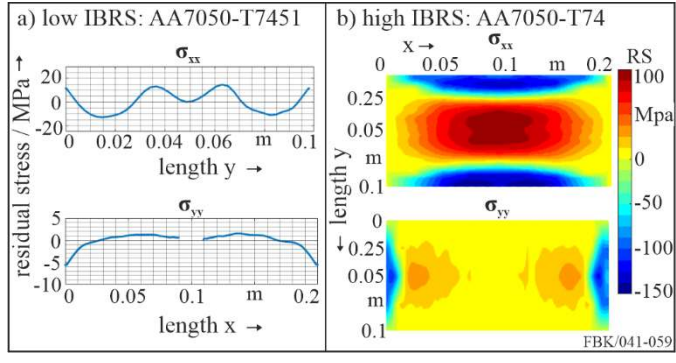


Fig. 4. Measured IBRS for low (a) and high (b) stress conditions

#### 2.2. Simulation

A static, linear elastic finite element model was set up in ABAQUS<sup>1</sup> to simulate the distortion due to the measured RS. The MIRS and the IBRS were implemented as an input and the distortion was calculated, after equilibrium had been set. The geometry was the same as in experiments (see Fig. 5). The z-direction corresponds to the depth of the MIRS. The measured MIRS (plane stress:  $\sigma_{xx}$ ,  $\sigma_{yy}$ ,  $\tau_{xy}$ ) were linearly interpolated over

depth z at the element centroids and applied as an initial condition (type = stress) in the boundary layer of the entire milled surface of the bottom of the pockets, of the backside and top of the sample. For depths smaller than the first measured point the first measured MIRS was used. For depths greater than the last measured depth, the measured in-plane IBRS ( $\sigma_{xx}$ ,  $\sigma_{yy}$ ) were linearly interpolated accordingly to their x- and y-position (see also Fig. 4). The mesh consisted of 245,739 eight-node brick elements (C3D8) for 3 mm wall thickness and 485,460 for 7 mm. The global size of the elements was set to 1.5 mm. The mesh was refined at the machined surfaces in z-direction in order to precisely resolve the MIRS. A coarser mesh was used in other regions to reduce the total number of elements for calculation time reasons. The part was constraint by the 3-2-1 constrain principle, which avoided rigid body motion, but enabled a free distortion of the body (see Fig. 5) [6]. Linear elastic material behavior with a Young's modulus of 71,700 MPa and a Poisson ratio v of 0.33 was given. After equilibrium was calculated, the displacement at the backside was analyzed similar to experiments (leveling and shifting data) and compared to the measured distortion.

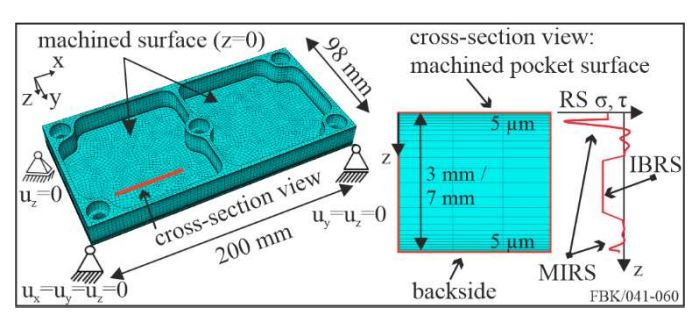


Fig. 5.FEM distortion prediction model [modified from 15]

### 3. Results and discussion

#### 3.1. Experiment

Fig. 6 exemplarily shows the color maps of the distortion (Post minus Pre) of one sample for each configuration. They mimic looking down at the milled surface of the pockets with positive distortion in the z-direction (into the surface). Fig. 7 exemplarily displays the distortion on both diagonals of the low IBRS sample L3M3A, and Fig. 8 shows the average diagonal distortion for each configuration. A general comparison of the distortion of the low and high IBRS samples (independent of their wall thickness and machining mode) shows that their distortion shape and magnitude differ (see Fig. 6). The high IBRS samples become convex (\(\capsilon\)-shaped) and the maximum distortion can be found towards the edges. The magnitude of the maximum distortion is around 0.6 mm. In contrast to the high IBRS samples the lowest level of distortion of the low IBRS samples is not in the middle of the sample. A X-shaped distortion is found with its maximum distortion near the top left (0 mm, 0 mm) and bottom right corner (200 mm, 98 mm), which is about 0.12 mm for L3M3A, and its minimum at the other two corners. This shows that for high IBRS samples the IBRS are driving the distortion, because their RS are much higher and they are contained in the entire bulk of the sample (see Fig. 4). The removal of the material leads to a disequilibrium of the IBRS. The distortion is the result of the stresses

gaining equilibrium again [19]. A closer look at the low IBRS samples (L3M1A, L3M3A) reveals that for both machining modes the distortion shape looks alike. However, the aggressive machining, inducing more MIRS deeper into the material, leads to higher distortions (see Fig. 6, 8). The shear MIRS are responsible for this X-shaped distortion with the maximum distortion close towards the two opposite edges. They cause a torsional moment, due to the zig milling strategy, in addition to the bending moment caused by the normal RS [20].

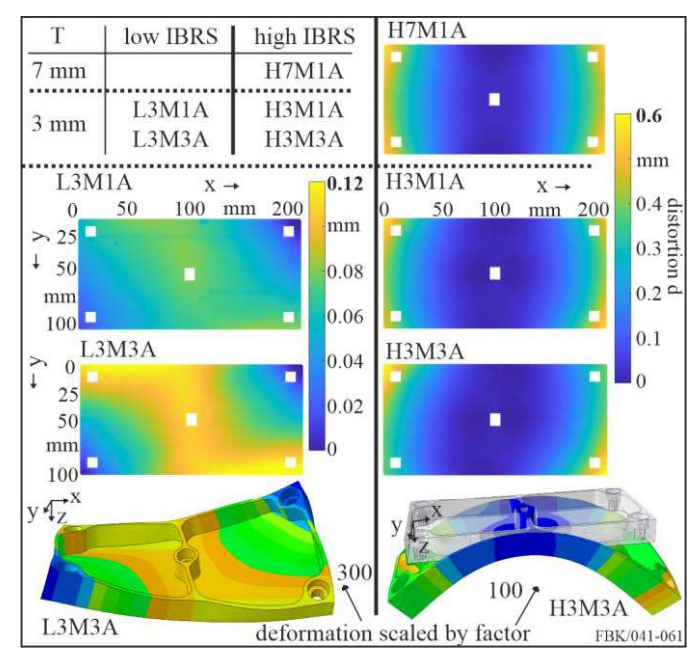


Fig. 6. Color maps of distortion for all configurations

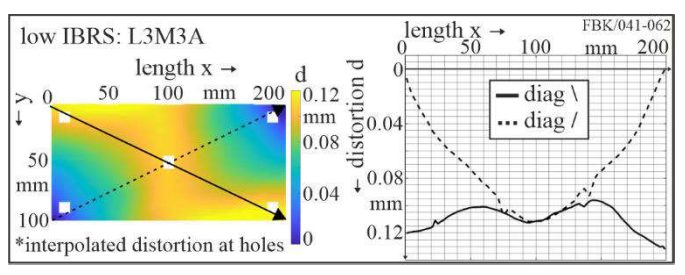


Fig. 7. Color map and diagonal distortion for L3M3A

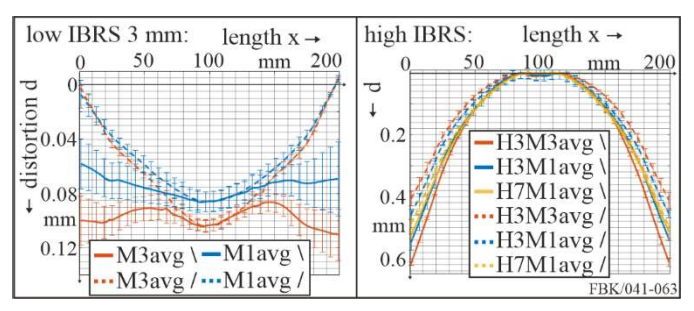


Fig. 8. Average diagonal distortion of each configuration (3 samples for each config.), error bars represent standard deviation; mind the different scales

The comparison of the high IBRS samples with different wall thicknesses (H7M1, H3M1) shows that their distortion shape looks alike with similar magnitude (see Fig. 6, 8). However, a closer look reveals that for the 3 mm sample, the previously-mentioned twisted behavior of distortion with its maximum distortion at two opposite corners is visible. This is due to the shear MIRS. This effect gets even more obvious for the samples of the same thickness, but machined with M3

(H3M3A). The higher and deeper MIRS lead to an even more twisted shape compared to M1. The maximum distortion is slightly higher (see Fig. 8). But the IBRS are still the dominating cause for the magnitude of the distortion.

Fig. 8 contains the average diagonal distortion of three repetitions per configuration with its standard deviation. In general, one can say that machining causes repeatable distortions with a high accuracy for high IBRS samples and lower accuracy for low IBRS, due to their lower distortion level. But above discussed trends are repeatable.

#### 3.2. Simulation

Fig 9 shows the color maps of the simulated distortions for the different configurations. It can be seen that the simulation model is able to predict the shape of distortion qualitatively for all different configurations. All the different effects discussed in section 3.1, such as the X-shape for low and the  $\cap$ -shape of distortion for high IBRS, are covered by the simulation. Furthermore, the magnitudes of distortion for simulated and measured distortions are on a similar level. One exception is L3M1. Here the level of distortion is underestimated by the simulation. Fig. 10 shows the comparison of the diagonal distortions of experiment and simulation for each configuration in detail. The prediction of the distortion of configuration L3M3 is close to the experimental data (see Fig. 10a). The maximum distortion found on one of the diagonals of the simulation accounts for 116 % compared to the maximum of the average experimental diagonal data. The L3M1 maximum diagonal distortion is reached by 67 % by the simulation. The maximum of the high IBRS distortions are predicted by a higher accuracy: H3M3 configuration is predicted by 94 %, H3M1 by 95 % and H7M1 by 93 % (see Fig. 10b, c, d).

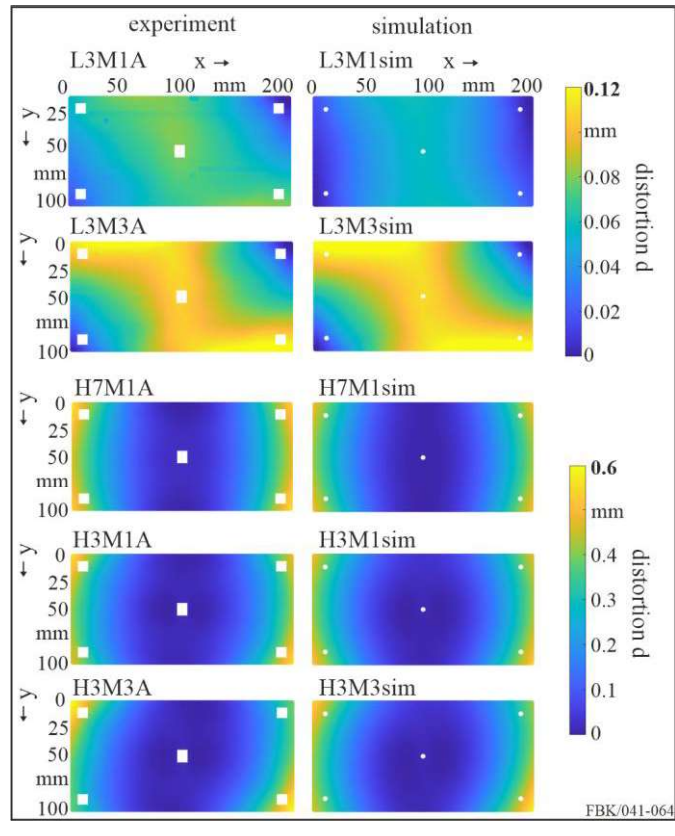


Fig. 9. Color maps of measured and predicted distortion for all configurations

In general, the accuracy of the prediction of low IBRS configuration, especially combined with low MIRS (L3M1), is lower, because little variations/errors in the HD measurements for measuring the MIRS have more impact on the distortion of low IBRS samples than for high IBRS samples. Here it should be mentioned, that the HD measurements of M1 have their maximum absolute value of compressive MIRS at the first measured depth, nearest to the surface (see Fig.2), where the uncertainty of the HD technique itself is the highest [14]. Although the MIRS produced by face milling the backside and top of samples is relatively low compared to the MIRS resulting from milling the pockets (see Fig. 3), they have a certain influence on the distortion of the low IBRS. The fact that measuring really low MIRS with the HD technique (consider relatively high standard deviation in Fig. 3), contributes to the difference of simulated and measured distortion of the configuration L3M1. Besides, MIRS in the rib and walls were not considered.

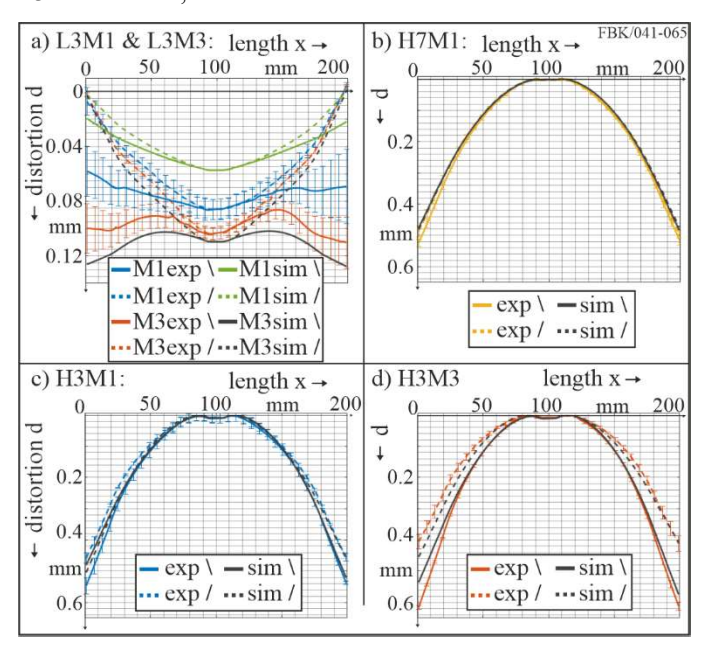


Fig. 10. Experimental and predicted diagonal distortion of low stress samples (a) and high stress samples with shifted distortion to 0 at center (b, c, d)

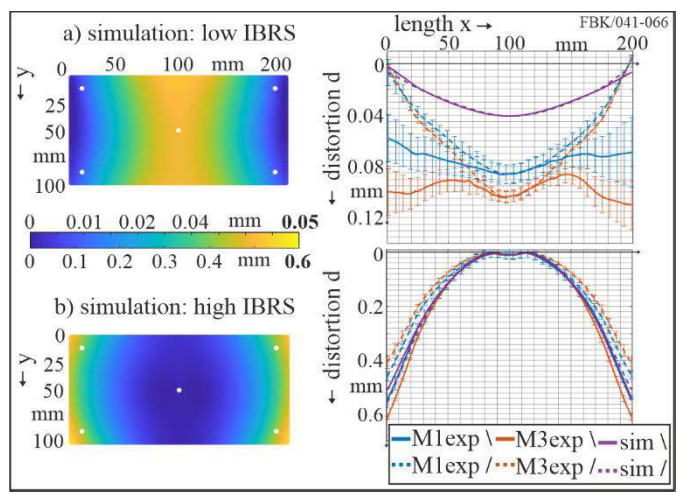


Fig. 11. Predicted distortion due to only low (a) and only high IBRS (b) for 3 mm thick samples and their diagonal distortion compared to experiments

Fig. 11 shows the distortion of simulations, where only the IBRS were applied as an initial condition and no MIRS were used. This should answer the question whether MIRS or IBRS

are the driving factor for the distortion when comparing these results to the previously discussed distortions.

A comparison of Fig 11a to Fig. 9 shows that the distortion shape resulting only from the low IBRS does not match the experimental results that include MIRS. Furthermore, the level of distortion is too small, especially compared to L3M3 (mind the different scales). This means that the driving factor for the distortion of milled low IBRS parts (3 mm) are the MIRS with respect to the used milling strategy. But the bulk stresses still contribute to the level of distortion.

A comparison of Fig 11b to Fig. 9 shows that the distortion shape resulting only from the high IBRS is similar to the distortion caused by the superposition of MIRS and IBRS. The shape and level of distortion match, which means that the driving factor for the distortion of milled high IBRS parts are the IBRS. However, the MIRS contribute to the shape of distortion, especially for the high MIRS (H3M3) where the maximum of distortion is found only on two opposite corners instead of all four (see Fig. 9 and section 3.1).

Fig. 12 highlights the distortion of simulations of L3M3, where the shear RS were neglected (a) and only the shear RS (without normal RS) (b) were used as an input. It can be seen, that the shear RS are crucial for the shape and level of distortion with respect to the used milling strategy (compare to Fig. 9 and 10).

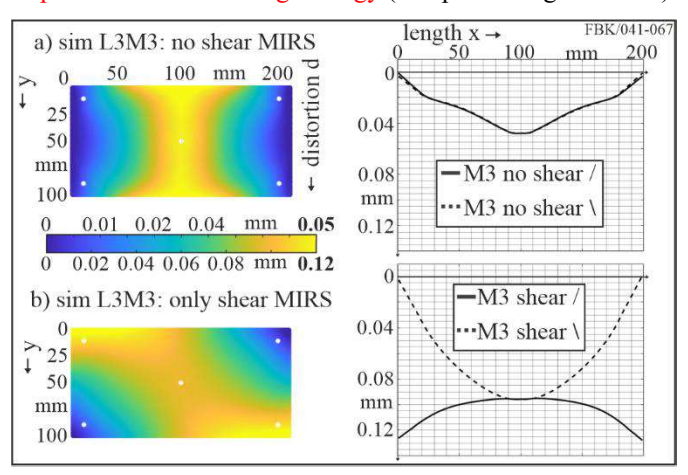


Fig. 12. Predicted distortion without considering shear MIRS (a) and only considering shear MIRS for L3M3 configuration; mind different scales

## 4. Conclusion

It can be stated that the main factor for distortion of AA7050-T74 parts, which have not undergone a stress relief process and therefore containing high IBRS, are only these IBRS. Nevertheless, there is a systematic influence of the combined effect of both stress types found for thin wall thicknesses (3 mm). The main driver for the distortion of milled stress relieved AA7050-T7451 thin walled parts, containing low IBRS, are the MIRS. But the bulk stresses still contribute to the level of distortion. It is found that the shear stress induced by machining is crucial for the distortion. The developed FEM model is able to predict the distortion due to both measured RS types.

In future research, models to predict the RS and the analysis of compensation methods to minimize distortion are planned.

# Acknowledgements

The authors would like to thank the German Research Foundation (DFG) and the National Science Foundation (NSF) for the financial support within the project AU 185/64-1 "NSF

DFG Collaboration to Understand the Prime Factors Driving Distortion in Milled Aluminum Workpieces" (NSF funding Award No. 1663341). Any opinions, findings, and conclusions or recommendations expressed in this material are those of the authors and do not necessarily reflect the views of the DFG or NSF. 'Naming of specific manufacturers is done solely for the sake of completeness and does not necessarily imply an endorsement of the named companies nor that the products are necessarily the best for the purpose.

#### References

- [1] Denkena B, Dreier S. Simulation of residual stress related part distortion. In New Production Technologies in Aerospace Industry - Proceedings of the 4th Machining Innovations Conference, Hannover; 2014. p. 105–113.
- [2] Jayanti S, Ren D, Erickson E, Usui S, Marusich T, Marusich K, Elanvogan H. Predictive modeling for tool deflection andpart distortion of large machined components. In Procedia CIRP 12 Proceedings of the 8th CIRP Conference on Intelligent Computation in Manuf. Eng. 2013; 37–42.
- [3] Yang Y, Li M, Li KR. Comparison and analysis of main effect elements of machining distortion for aluminum alloy and titanium alloy aircraft monolithic component. Int J. Adv. Manuf. Technol. 2014; 70/9:1803-1811.
- [4] Sim WM. Challenges of residual stress and part distortion in the civil airframe industry. Int J Micro-struct Mater Prop 2010; 5:446–455.
- [5] Li JG, Wang SQ. Distortion caused by residual stresses in machining aeronautical aluminum alloy parts: recent advances. Int J Adv Manuf Technol 2016; 89:997–1012.
- [6] Huang XM, Sun J, Li JF. Finite element simulation and experimental investigation on the residual stress-related monolithic component deformation. Int J Adv Manuf Technol 2015; 77:1035–1041.
- [7] Huang XM, Sun J, Li JF. Effect of initial residual stress and machininginduced residual stress on the deformation of aluminium alloy plate. Journal of Mechanical Engineering 2015; 612:131–137.
- [8] Richter-Trummer V, Koch D, Witte A, dos Sanos JF, de Castro PMST. Methodology for prediction of distortion of workpieces manufactured by high speed machining based on an accurate through-the-thickness residual stress determination. Int J of Adv Manuf Tech 2013; 68:2271–2281.
- [9] Dreier S. Simulation des eigenspannungsbedingten Bauteilverzugs. Disseratation 2018.
- [10] Madariaga A, Perez I, Arrazola PJ, Sanchez R, Ruiz JJ, Rubio FJ. Reduction of distortions in large aluminum parts by controlling machininginduced residual stresses. Int J Adv Manuf Technol 2018; 97: 967-978.
- [11] Ma Y, Zhang J, Yu D, Feng P, Xu C. Modeling of machining distortion for thin-walled components based on the internal stress field evolution. Int J Adv Manuf Technol 2019; 103:3597-3612.
- [12] ASM Handbook: Heat Treating of Aluminum Alloys. 1991; 4:841-879.
- [13] ASTM International. E837-13a Standard Test Method for Determining Residual Stresses by the Hole-Drilling Strain-Gage Method. West Conshohocken, PA: ASTM International; 2013.
- [14] Chighizola CR, D'Elia CR, Weber D, Kirsch B, Aurich JC, Linke BS, Hill MR. Intermethod Comparison and Evaluation of Measured Near Surface Residual Stress in Milled Aluminum. *Currently under review* in Expermintal Mechanics, Submitted April 2020.
- [15] Weber D, Kirsch B, Chighizola CR, Jonsson JE, D'Elia CR, Linke BS, Hill MR, Aurich JC. Finite element simulation combination to predict the distortion of thin walled milled aluminum workpieces as a result of machining induced residual stresses. Proceedings of the 2nd Int. Conference of the DFG IRTG 2057 Physical Modeling for Virtual Manufacturing (iPMVM 2020), OASIcs 89. 2021.
- [16] Hill MR. The slitting method. In: Schajer GS (ed). Practical residual stress measurement methods. Wiley, West Sussex, UK; 2013.
- [17] Olson MD, Hill, MR. Two-Dimensional Mapping of In-plane Residual Stress with Slitting. Exp Mech 2018; 58: 151-166.
- [18] Garcia DR, Hill MR, Aurich, JC, Linke BS. Characterization of machining distortion due to residual stresses in quenched aluminium. In 12th Int. Manuf. Science and Engineering Conference (1), MSEC2017-2878; 2017.
- [19] Masoudi S, Amini S, Saeidi E. Effect of machining-induced residual stress on the distortion of thin-walled parts. Int J Adv Manuf Technol 2015; 76: 597–608.
- [20] Gulpak M, Sölter J, Brinksmeier E. Prediction of shape deviations in face milling of steel. In Procedia CIRP 8 - Proceedings of the 14th CIRP Conference on Modelling of Machining Operations 2013; 15–2.

## Available online at www.sciencedirect.com



# ScienceDirect

Procedia CIRP 00 (2019) 000-000

